Received: 2 April 2019 | Revised: 25 October 2019 | Accepted: 26 October 2019

DOI: 10.1111/jace.16886

Journal of the American Ceramic Society

ORIGINAL ARTICLE

Size-induced grain boundary energy increase may cause softening of nanocrystalline yttria-stabilized zirconia

Arseniy Bokov[1] | **Joao B. Rodrigues Neto**[1,2] | **Feng Lin**[3] | **Ricardo H. R. Castro**[1]

[1]Department of Materials Science and Engineering, University of California, Davis, Davis, CA, USA

[2]Graduate Program on Materials Science and Engineering (PGMAT), Federal University of Santa Catarina, Florianópolis, SC, Brazil

[3]School of Chemical Engineering and Technology, Sun Yat-sen University, Zhuhai, China

Correspondence
Ricardo H. R. Castro, Department of Materials Science and Engineering, University of California, Davis, Davis, CA 95616, USA.
Email: rhrcastro@ucdavis.edu

Funding information
Conselho Nacional de Desenvolvimento Científico e Tecnológico, Grant/Award Number: 303569/2015-8; Army Research Office, Grant/Award Number: W911NF-17-1-0026

Abstract

An increase in hardness with reducing grain sizes is commonly observed in oxide ceramics in particular for grain sizes below 100 nm. The inverse behavior, meaning a decrease in hardness below a critically small grain size, may also exist consistently with observations in metal alloys, but the causing mechanisms in ceramics are still under debate. Here we report direct thermodynamic data on grain boundary energies as a function of grain size that suggest that the inverse relation is intimately related to a size-induced increase in the excess energies. Microcalorimetry combined with nano and microstructural analyses reveal an increase in grain boundary excess energy in yttria-stabilized zirconia (10YSZ) when grain sizes are below 36 nm. The onset of the energy increase coincides with the observed decrease in Vickers indentation hardness. Since grain boundary energy is an excess energy related to boundary strength/stability, the results suggest that softening is driven by the activation of grain boundary mediated processes facilitated by the relatively weakened boundaries at the ultra-fine nanoscale which ultimately induce the formation of an energy dissipating subsurface crack network during indentation.

KEYWORDS

grain boundaries, hardness, nanomaterials, zirconia: yttria stabilized

1 | INTRODUCTION

The strong resistance to plastic deformation in most ceramic materials originates from the character of the chemical bonds and the limited density of dislocation slip planes which do not allow for appreciable nucleation and mobility of dislocations under normal conditions.[1] Grain size refinement, with the resulting expansion of the grain boundary network, may act as an additional effective barrier for dislocations, further reducing plasticity and increasing hardness—often referred to as Hall-Petch relation.[2] In ceramics, this behavior is more pronounced when grain sizes are below 100 nm, but as grain sizes are further reduced, several studies also report, instead, the existence of an inverse relation as grains are refined below a critical size.[3–8]

Although still being topic of discussion in the literature, this so-called inverse Hall-Petch relationship has been associated in metal alloys with load accommodation by grain boundary sliding and other grain boundary mediated diffusion process only activated for very small grain sizes.[9] While this seems to be the effective mechanism in metal alloys, in ceramics the inverse relation has been also attributed to the increase in the fraction of tiple junctions that allow for a change in energy dissipation and fracture behavior.[5] This result implies the inverse relation is not a diffusion-based process but rather related to the activation of new energy dissipation modes.

When the grain size in a dense material is reduced to the nanoscale, geometrical constrains may significantly affect the structural nature of the grain-grain interfaces due to a large population of triple junctions and high density of kinks—all potentially increasing the excess energy of the grain boundary. Therefore, as the grain size is reduced, the value of the specific grain boundary energy may be increased due to the

increased triple joint population and the fact that the ratio of grain boundary to corner area is closer to unity. Moreover, it has been extensively reported that the grain boundary energy is expected to be lower for larger grained materials simply as a result of the change in grain boundary orientation population.[10,11] As the grains grow, the density of high energy grain boundaries decreases since these have higher driving force for movement, leaving an increased population of the more stable low energy grain boundaries in large-grained samples. Such changes shall lead to higher energy boundaries at the nanoscale, which could translate into reduced strength (or toughness, or stability), since the strength of boundaries has been directly related to its energy in previous works, either considering its chemistry[12] or the orientation of boundaries.[13]

The connection between grain boundary stability and inverse Hall-Petch has been reported by Hu et al for Ni-Mo alloys.[2] In principle, as the grain boundaries show low stability against plastic straining, the deformation mechanisms in this alloy shift from dislocation slip to grain boundary-mediated processes, leading to the observed decay in hardness. On the other hand, in nanocrystalline alloys with inherent high grain boundary stability (low grain boundary energy), grain boundary-mediated processes are inhibited, resulting in substantial hardening with a postponed inverse Hall-Petch relation.

In this work, we explored the grain boundary energy dependence on grain size at the nanoscale utilizing yttria-stabilized cubic zirconia (10YSZ) as a model ceramic system. To achieve this, fully dense 10YSZ pellets with different grain sizes were produced using high pressure spark plasma sintering (HP-SPS) and varying the processing conditions. Direct calorimetric measurements of grain boundary energies were performed and correlated with Vickers hardness measured in each individual sample. Grain boundary energy increase (weakening) is observed at the onset point of the inverse Hall-Petch relation. By studying cross sections of the hardness indentations produced by focused ion beam, it is suggested that such size-induced softening is related to a load accommodation by subsurface branched fracture, consistent with Ryou et al who proposed the activation of novel energy dissipation mechanisms below critical sizes.[5]

2 | EXPERIMENTAL PROCEDURES

2.1 | Synthesis of nanocrystalline 10YSZ powder

Nanocrystalline powders of yttria-stabilized zirconia were synthesized through the reverse precipitation route.[14,15] The starting reagents, zirconium oxynitrate hydrate (Sigma Aldrich, 99%) and yttrium nitrate hexahydrate (Alfa Aesar, 99.9%), were dissolved in deionized water to form a 0.75 mol/L aqueous solution. The obtained liquid was gradually dripped into high excess of 5 mol/L ammonia solution. A magnetic stir bar was placed into the ammonia beaker to ensure a strong basic environment for each droplet of the nitrates. The direct contact between two liquids initiated the reaction between ammonium hydroxide and nitrate salts which resulted on the precipitation of Zr-Y hydroxide nuclei. The obtained hydroxide precursor was then separated from the excess ammonia by centrifuging in plastic bottles and washed by additional centrifuging with ethanol three times. The resulting slurry was kept in a drying oven at 80°C for 48 hours. After drying, the chunks of the hydroxide precursor were crushed in a mortar and calcined at 450°C in ambient air for 2 hours for the formation of oxide nanoparticles of ZrO_2 with 10 mol% Y_2O_3 (10YSZ).

2.2 | Spark plasma sintering of nanocrystalline YSZ powders

The obtained nanopowders of yttria-stabilized zirconia were degassed at 400°C for 16 hours in Smart VacPrep (Micromeretics) and transferred to a glove box filled with dry nitrogen to keep moisture away from the surface of the nanoparticles. For high pressure spark plasma sintering (HP-SPS) experiments, the powder was loaded into the inner cylindrical die with 4mm in diameter made of Versimax™ (Hyperion Materials & Technologies, Sandvik) which is a composite of diamond and silicon carbide. The plungers of the same material were placed on the top and on the bottom of the inner die in order to transfer the load. The resulting assembly was placed into the outer graphite die to ensure a sufficient electrical conductivity.

The sintering was performed in a SPS apparatus 825S (SPS Syntex Inc) under medium vacuum conditions (about 10^{-2} Torr). The maximum temperature and pressure were varied in the range of 920°C-1070°C and 800-2100 MPa, respectively, to produce fully dense samples with different grain sizes. There was no isothermal hold at the maximum temperature, so that densification was happening only during the thermal ramp. After HP-SPS, all samples were reoxidized and strain-relaxed for 1 hour at 150°C below the maximum sintering temperature. In total, two similar sets of samples were produced to analyze the evolution of thermodynamic and mechanical properties as a function of grain size.

2.3 | Measurements of excess grain boundary energy

The sintered ceramic pellets were subjected to Differential Scanning microCalorimetry (DSC)[16] using a Netzsch DSC404 Pegasus (Netzsch GmbH) in order to assess the thermodynamic properties of grain boundaries. The samples with different grain

sizes were heated up in argon at 20°C/min up to a maximum temperature of about 1100°C-1300°C with subsequent 10 minutes of isotherm to activate grain growth. The observed heat signals were normalized by the change in grain boundary area in order to calculate the grain boundary energy, as described in validated protocols.[15–18] Noteworthy, when determining the excess energy from those DSC protocols, the total excess heat measured in the calorimeter is attributed exclusively to the actual change in grain boundary area. However, the excess energy can and will include other defects, for instance, triple junctions and vacancies that are also being removed during annealing. That said, the relative area and amount of such defects is much smaller than the contribution of interfaces themselves. The initial and final grains sizes, ie, before and after the heat release, were analyzed by Scanning Electron Microscopy (SEM) on a FEI Nova NanoSEM430 (Thermo Fisher Scientific) and by X-ray Powder Diffraction (XRD) on a Bruker-AXS D8 Advance Diffractometer (Bruker Inc). In total, about 400-700 grains imaged in different areas were used to calculate the average grain size of each of the samples.

2.4 | Measurements of Vickers hardness

The obtained samples of sintered 10YSZ were polished down to 100 nm diamond paste to ensure flat smooth surfaces. The indentations were performed with a Vickers pyramid on a Mitutoyo HM-220A (Mitutoyo Corporation) using 20, 40 and 60 g of load (gf). The resulting hardness impressions were imaged using SEM on a FEI Nova NanoSEM430 (Thermo Fisher Scientific). About 12-16 indentations, without any spallation, were imaged under SEM for each of the loads exerted onto the samples with different grain sizes (about 300 SEM images). It is important to note that spallations would result in reduction in the measured hardness, as reported by Ryou et al.[5] This work focused on spallation free indentation.

2.5 | Microscopy

To investigate the mechanisms of deformation during indentation experiments, sectioning of some indents was accomplished on a Scios DualBeam SEM/FIB (Thermo Fisher Scientific). At first, a 1 micron-thick tungsten coating was deposited onto the indents to protect the area of interest from the ion beam damage. Thereafter, a gradual removal of the material was performed by the Ga-ion beam with 30 kV of accelerating voltage and 5 nA of current. Furthermore, micropillar samples with thinned central regions were prepared for in situ transmission electron microscopy (TEM) based mechanical testing. A central region of the micropillar with about 1.5 μm was thinned down to thickness below 100 nm to enable observation of the cracks with respect to the grains. The thinning was performed using sequential milling with Ga^+ focused ion beam culminating with 7.7 nA at 30 kV. Previous studies on the effect of FIB conditions in stabilized zirconia have shown that 30 kV at such relatively low currents effectively leads to negligible damage,[19] what can be attributed to the inherent high resistance of zirconia to ion irradiation damage at the used energy level.[20,21]

Cracks were induced in situ by compression loading at the thinned area using a flat diamond punch with 1 μm in diameter displaced at a constant rate of 0.1 nm s^{-1} (Hysitron PI-95 Picoindenter). In-situ imaging was obtained during loading in a JEOL 2100 Cryo TEM (although the cryogenic function was not utilized). The picoindenter dimension is smaller than the total thinned area, guaranteeing all load is transferred to the <100 nm zone. Cracks were observed to initiate at the bottom of the indenter, where the maximum stress is being applied and consistent with micro-indentation experiments.

3 | RESULTS AND DISCUSSION

3.1 | Nanocrystalline ceramics preparation

The average grain sizes for the produced samples and the corresponding heating and loading conditions used in SPS are shown in Table 1. All reported conditions resulted in relative density above 99.9% (as measured by Archimedes method following ASTM B311-13 standard) and other conditions that did not lead to similar levels of densification are not shown. The table reports the whole sintering profile with the respective grain size, including temperature ramping, pressure increase rate and final temperature. No holding time was utilized and the equipment was shut down when the maximum listed temperature and pressure were reached (bold text in the Table 1). The sintering profiles are the result of extensive empirical tests, and the obtained values of grain sizes were purposely targeted to ensure a spread of the data points. One can observe that the sintering profile allowed for a refined control over the final grain size by means of varying pressure and temperature, and grain sizes ranging from 16 to 48 nm were obtained. The smallest grain sizes required excessively high pressures, up to 2.1 GPa, with the decreasing pressure and pressure holding time being associated with enlarged grain sizes. The largest grain size was produced at about 800 MPa. The additional specimen for mechanical testing with the grain size of about 100 nm was produced by annealing of the 48 nm sample at 1200°C for 15 minutes to trigger some limited grain growth.

3.2 | Thermodynamic measurements

The set of samples listed on the top of Table 1 were used to measure the grain boundary energy of 10YSZ by microcalorimetry.

TABLE 1 The average grain sizes for the produced samples of 10YSZ and corresponding heating and loading profiles used in spark plasma sintering

Grain size	Heating profile	Loading profile							
10YSZ samples for differential scanning microcalorimetry									
16.2 ± 0.9 nm	to 650°C in 7 min	to **920°C** in 11 min	120 MPa at 7 ½ min	430 MPa at 8 ½ min	870 MPa at 9 ½ min	1300 MPa at 10 ½ min	1600 MPa at 11 ½ min	1900 MPa at 12 ½ min	**2100 MPa** at 13 ½ min
20.1 ± 1.1 nm	to 700°C in 7 min	to **965°C** in 10 min	120 MPa at 8 min	430 MPa at 9 min	870 MPa at 10 min	1150 MPa at 11 min	1450 MPa at 11 ½ min	**1700 MPa** at 12 ½ min	
25.7 ± 1.5 nm	to 830°C in 8 min	to **1030°C** in 10 min	120 MPa at 9 min	430 MPa at 10 min	870 MPa at 11 min	1050 MPa at 11 ½ min	**1180 MPa** at 12 ½ min		
10YSZ samples for mechanical testing									
16.8 ± 0.9 nm	to 660°C in 7 min	to **925°C** in 11 min	120 MPa at 7 ½ min	430 MPa at 8 ½ min	870 MPa at 9 ½ min	1300 MPa at 10 ½ min	1600 MPa at 11 ½ min	1900 MPa at 12 ½ min	**2100 MPa** at 13 ½ min
19.1 ± 1.0 nm	to 700°C in 7 min	to **960°C** in 10 min	120 MPa at 8 min	430 MPa at 9 min	870 MPa at 10 min	1150 MPa at 11 min	1450 MPa at 11 ½ min	**1700 MPa** at 12 ½ min	
21.4 ± 1.2 nm	to 710°C in 7 min	to **970°C** in 10 min	120 MPa at 8 min	430 MPa at 9 min	870 MPa at 10 min	1150 MPa at 11 min	1450 MPa at 11 ½ min	**1700 MPa** at 12 min	
27.3 ± 1.6 nm	to 840°C in 8 min	to **1040°C** in 10 min	120 MPa at 9 min	430 MPa at 10 min	870 MPa at 11 min	1050 MPa at 11 ½ min	**1250 MPa** at 12 min		
36.3 ± 2.5 nm	to 900°C in 8 min	to **1090°C** in 9 min	120 MPa at 9 min	430 MPa at 10 min	870 MPa at 11 min	**1000 MPa** at 11 ½ min			
47.7 ± 3.2 nm	to 950°C in 9 min	to **1140°C** in 8 min	120 MPa at 9 ½ min	430 MPa at 10 ½ min	**800 MPa** at 11 ½ min				

Bold represents the final (maximum) temperature and pressure reached during the processing cycle.

TABLE 2 List of DSC experiments that was used to extract the grain boundary energy in 10YSZ as a function of grain size

Max. Temp. & DSC notation	Grain size, nm		Grain boundary area, m^2/g		
	Initial	Final	Initial	Final	ΔH_{DSC}, J/g
1095°C "16 → 36"	15.9 ± 0.9	35.8 ± 2.2	34.1	15.2	19.94 ± 1.02
1150°C "20 → 64"	20.0 ± 1.1	63.9 ± 4.7	25.4	7.9	15.71 ± 0.79
1155°C "16 → 64"	16.3 ± 0.9	63.7 ± 4.6	31.1	8.0	21.78 ± 1.03
1290°C "26 → 225"	25.7 ± 1.5	222 ± 15	20.6	2.4	12.80 ± 0.76
1295°C "20 → 225"	20.2 ± 1.1	227 ± 13	26.8	2.4	19.89 ± 1.19
1300°C "16 → 225"	16.3 ± 0.9	225 ± 14	32.4	2.3	26.09 ± 1.04

Note: Samples were heated 20°C/min to the temperature indicated in the first column followed by the isothermal hold at this temperature for 10 min. The first column also shows the associated notation used in the legend of Figure 1.

The prepared samples were exposed to grain growth during temperature ramping inside the DSC and up to different maximum temperatures. Grain growth is an exothermic process which is related to elimination of grain boundary area. Therefore, each experiment provides the average energy in a specific range of grain sizes according to the following Equation (1):[16]

$$\gamma_{\text{initial}} \cdot \text{GBA}_{\text{initial}} - \gamma_{\text{final}} \cdot \text{GBA}_{\text{final}} = \Delta H_{\text{DSC}}. \quad (1)$$

Here, ΔH_{DSC} is the heat signal obtained from DSC, γ is the excess grain boundary energy in the initial or final grain sizes ("final" is defined as the state after the exothermic peak of grain growth), and *GBA* stands for the associated value of grain boundary area in the particular state. In the general case, the surface energy could also be included in this Equation, but the term is omitted here due to its negligible contribution for fully dense nanocrystalline samples.[22] The grain boundary area associated with a given grain size was calculated using the Equation (2):[15,16]

$$\text{GBA} = \frac{S}{d} \cdot \frac{V_{\text{M}}}{M} \cdot e^{-2.5(\ln \sigma)^2}. \quad (2)$$

Here, S is a shape factor set as 3.55 assuming tetrakaidecahedral grains,[23] d is the average grain size, V_{M} and M are molar volume and mass, respectively, and σ is the standard deviation of the normalized grain size as a correction factor to account for the distribution of sizes (which was determined experimentally by SEM). The tetrakaidecahedral shape is considered a reasonable assumption for grain shape based on the very high degree of

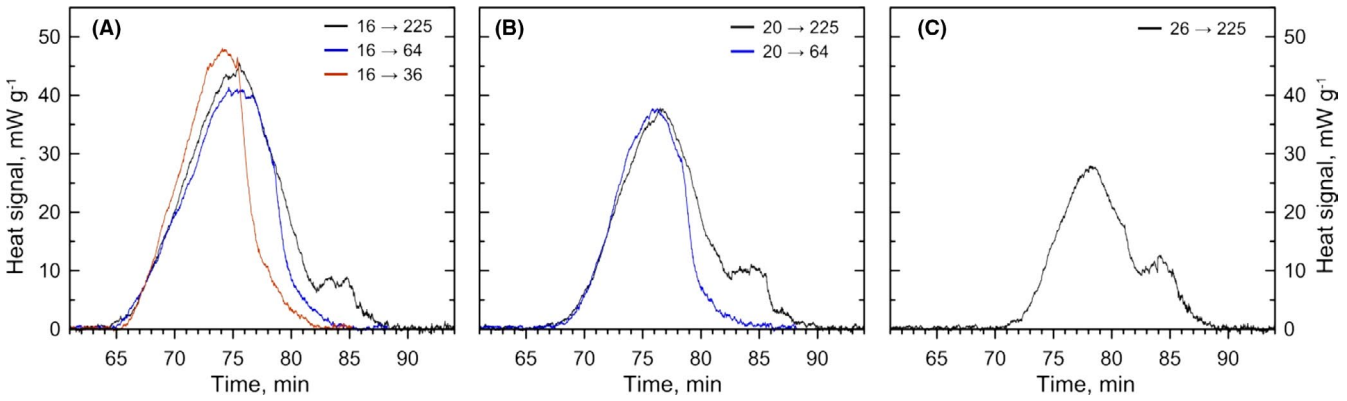

FIGURE 1 Exothermic heat effects associated with the release of grain boundary energy for a series of 10YSZ samples during grain growth, as detected by DSC analysis. The legend in the top-right corner of the graphs represents the change in the grain size (in nm) by the end of experiment. More details can be found in Table 2

crystallinity down to 10 nm grain size reported by in the literature,[24] and the consistent grain shapes observed in our studies via SEM.

Experimentally, one can reliably measure the heat signal as well as determine the grain boundary areas from samples quenched immediately before and after the DSC peak. However, Equation (1) does not allow for direct calculation of absolute grain boundary energies at each given grain size since it contains two variables: the grain boundary energies at the initial and final stages (which can differ). To remove these constrains, different initial grain sizes were utilized along with tuning of the final grain size by varying the maximum temperature of sintering in the DSC runs. Such approach increases the number of Equations but minimizes the number of variables. That is, three distinct starting grain sizes (three specimen with ~16 nm, two with ~20 nm, and one with ~26 nm) were used for calorimetric analysis at distinct temperatures (see Table 2). Note that efforts were made to perfectly match the sizes of each sample but there are intrinsic experimental variations that preclude this. Such sizes are assumed the same for the sake of calculations and the deviations are included in the error bars of the calculated energies.

Figure 1A shows the heat signals associated with grain growth of a set of ~16 nm samples heated up to the maximum temperatures of 1300°C, 1155°C, and 1095°C. These three different temperatures led to coarsening to distinct final grain sizes, ~225, ~64, and ~36 nm, respectively. Figure 1B shows data for ~20 nm samples heated to 1295°C and 1150°C and Figure 1C for 26 nm sample heated up to 1290°C. Slight changes in the final temperature were purposely designed so that samples with different starting grain size could match the same size after the peak.

While the heat signals for different experiments can be extracted simply by integration of the DSC curves from Figure 1, since the instrument was properly calibrated with sapphire heat capacity, the change in grain boundary area must be verified with the XRD and microscopy analyses. SEM images representing typical microstructures with different average grain sizes (initial and final) can be seen in Figure 2 for reference and exemplification purposes. All images are shown with the same scale bar to facilitate comparison. Normal grain growth takes place during the DSC runs so there are fairly equaxial grains without any visible porosity for any given sample. The XRD patterns associated with the same samples as those shown in Figure 2 are shown in Figure 3. Smaller sizes demonstrate a pronounced peak broadening, while larger sizes show narrow peaks. The results of the whole profile refinements are very consistent with the sizes observed by SEM, except in the 225 nm case, which was quantified only by microscopy due to the intrinsic limitation of the technique.

The results from DSC, SEM, and XRD allow for the determination of ΔH_{DSC}, $GBA_{initial}$, and GBA_{final} values and enable

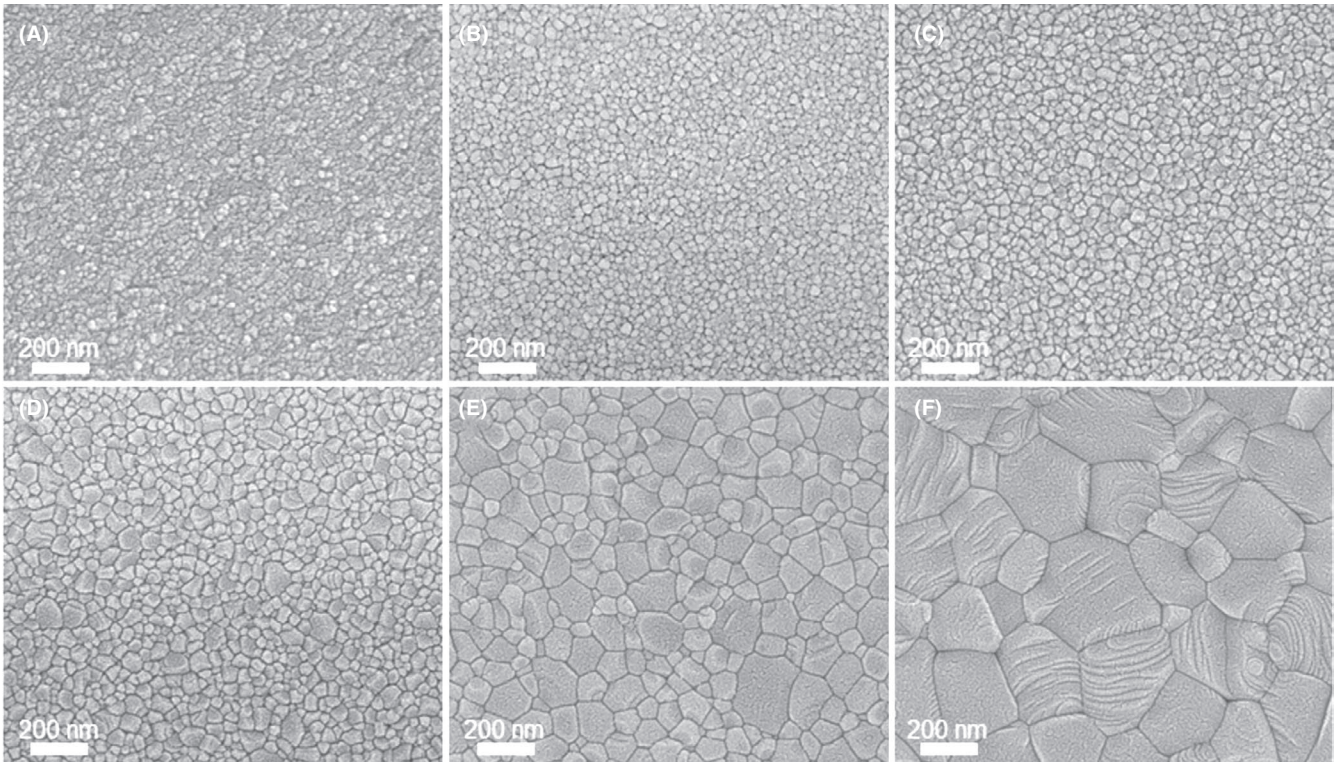

FIGURE 2 Typical SEM images for 10YSZ samples with the average grain sizes of roughly 16 nm (A), 20 nm (B), 26 nm (C), 36 nm (D), 64 nm (E), and 225 nm (F). Texture on the surface of the grains is a result of Au-Pd coating (1-2 nm thick) which was deposited onto the samples to mitigate charge accumulation during imaging or surface reconstruction during annealing

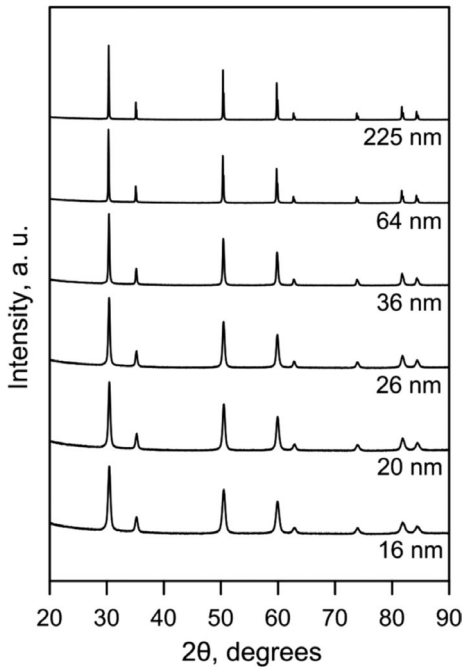

FIGURE 3 XRD patterns for 10YSZ samples with different grain sizes. No peaks other than for cubic fluorite phase are detected in all cases. Crystallite (grain) sizes are as indicated in the graph

the writing of a series of equations based on Equation (1). A comprehensive list of the utilized parameters is summarized in Table 2, and the equations can be written as follows:

$$\begin{aligned} 34.1\cdot\gamma_{16}-15.2\cdot\gamma_{36}&=19.9\\ 25.4\cdot\gamma_{20}-7.9\cdot\gamma_{64}&=15.7\\ 31.1\cdot\gamma_{16}-8.0\cdot\gamma_{64}&=21.8\\ 20.6\cdot\gamma_{16}-2.4\cdot\gamma_{225}&=12.8\\ 26.8\cdot\gamma_{20}-2.4\cdot\gamma_{225}&=19.9\\ 32.4\cdot\gamma_{16}-2.4\cdot\gamma_{225}&=26.1. \end{aligned} \tag{3}$$

Here, γ_x represents the grain boundary energy (units of J/m^2) at the grain size of x nm in size, ranging from 225 to 16 nm. Units and decimals are omitted in the equations for simplicity but shown in Table 2.

The unique solution for the energies for this system of equations was calculated using the least squares method and is shown with the left-side Y-axis in Figure 4. It can be seen that the grain boundary energy values do not significantly change for relatively large grains, having an average value of 0.56 J/m^2 for grains larger than 36 nm, which is consistent with the geometrical estimation of the modest interfacial area change in this grain size range. To evaluate if the thermodynamic values are reasonable, one may consider that about one-third of the grain boundary population in coarse-grained YSZ is represented by three dominant geometries[25]: Σ3 (11%), Σ5 (9%), and Σ11 (9%). The corresponding grain boundary energies for these orientations are 0.52, 1.03, and 0.25 J/m^2, respectively, as averaged from a few literature sources.[26,27] Considering fractions, the grain boundary energy resulting only from these geometries is 0.59 J/m^2, which is very close to the result obtained for larger grains in this study. Although the energy from just three grain boundaries is a clearly rough estimate, one should also consider that distribution of misorientation angles in cubic zirconia is likely centered on these dominant geometries.

The situation changes when the grain sizes are below ~36 nm, where a remarkable increase in grain boundary energy is observed (up to 0.84 ± 0.4 J/m^2 at 16 nm). This phenomenon can be attributed to a change in the grain boundary area and volume, with higher energy boundaries being more favorable to accommodate the geometry of such small grain sizes. Another possible explanation is the increase in the population of triple joints and density of kinks, assuming those increase the excess energy of the system. That is, although the heat from DSC is all inputted as grain boundary energy from using Equation (1), triple junction volume is more abundant at small grain sizes and may also be playing a significant role in the energy evolution. The calculations by Ryou et al,[5] however, indicate that the population of triple junctions is still small in the range where the increase in energy is observed. A recent study on ionic transport in cubic YSZ[28] has shown that the grain boundary width for this system is on the order of 0.5-1 nm. Further, according to Chaim,[29] the fraction of triple lines can be geometrically related to fqn = $3 \times 2(1 - x)$, where $x = (3/\sqrt{6}) \times$ (grain boundary thickness/grain size). Assuming, for instance, a 0.5 nm thick grain boundary, the triple junction population is indeed not significant at 36 nm (0.09%), or even at 16 nm (0.42%). If one considers a 1.0 nm thick grain boundary, the calculations indicate the onset size in which the increase in population of triple joints agrees with the onset of the grain boundary energy increase. The fraction of triple junction is increased to 0.34% at 36 nm, and 1.62% at 16 nm. Despite the onset coincidence, the actual fraction of triple junctions is very small.

Alternatively, one may attribute the change to a size-induced complexion transition, as suggested to exist in the nanostructured $MgAl_2O_4$.[30] The existence of such transition with two intrinsically different types of grain boundary area and volume is supported by the shape of DSC curves in Figure 1. Analyzing the peaks for the different starting grain sizes, one may note the samples exposed to temperatures up to 1100°C and 1150°C demonstrate only a single normal exothermic peak, whereas an additional peak 'shoulder' is clearly observed for all samples heated up to about 1300°C. This pattern suggests that some fraction of the grain boundaries becomes mobile only at higher temperatures. Although these boundaries might be already present in the sample from the beginning, it is also equally possible they are formed during the grain growth, ie, while transitioning from the nanoscale grain boundary type to the microscale

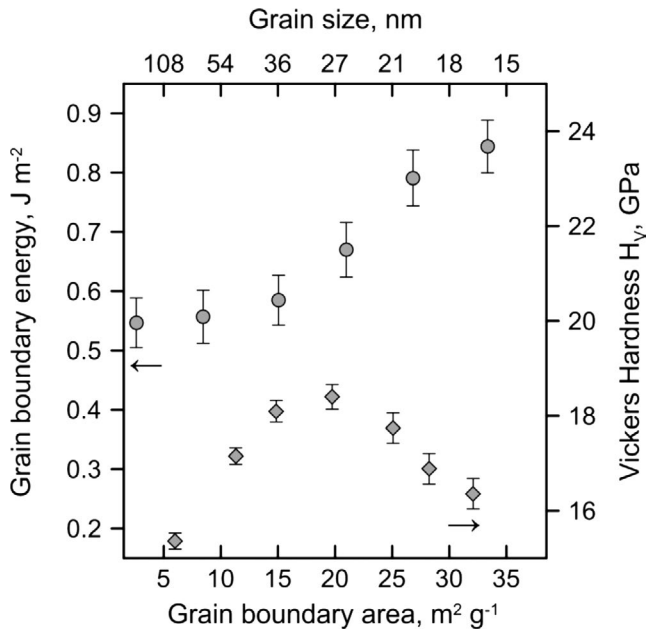

FIGURE 4 Evolution of grain boundary energy in 10YSZ (circles) as a function of grain boundary area (and grain size) along with the corresponding change in hardness of this compound (diamonds)

type. This is, of course, highly speculative at this point as it can also be related to impurities. Although their effective concentration at the grain boundaries should be very low due to a large grain boundary area, they can accumulate at specific grain boundaries in larger grained samples, leading to a mobility change. Noteworthy, one could argue that the existence of two different grain boundaries with different mobilities should lead to abnormal grain growth, which is not observed. However, this work deals with a very small grain size regime where the difference is observed, 15-30 nm. Therefore, even if there is a difference in mobility, there would not be time or conditions to cause abnormal grain growth to result in a nonnegligible microstructural observation in our studies. In any case, more systematic studies are required to determine the origin of the heat effect 'shoulder'. Therefore, the scope of the present work will be limited to the question of whether or not the observed trend in energetics of grain boundaries (or overall excess energy) can affect mechanical properties of the samples. For doing so, indentations with Vickers pyramid were performed on a set of nanocrystalline 10YSZ samples, as detailed in the experimental section.

3.3 | Mechanical properties

The results of hardness testing for indentations without spallations as a function of grain size are shown with the right-side Y-axis in Figure 4 along with the grain boundary energy data on the left-side Y-axis. As grain sizes decrease, hardness increases and reaches a maximum of 18.41 ± 0.26 GPa at the grain size of ~27 nm. Below this critical size, softening takes place and hardness decreases down to 16.36 ± 0.32 GPa at ~17 nm. It can be seen that the onset of the softening occurs at the same grain size range at which the increase in excess energy occurs for this oxide system. This behavior is consistent with the decrease in hardness reported for metallic alloys in grain sizes below 20 nm due to the abundance of boundaries with high excess energy[2] and activation of grain boundary-mediated deformation modes.[31,32]

To further study the possible mechanisms responsible for the inverse Hall-Petch in these samples, an analysis was performed focusing on the observed side cracks formed during indentation. The increased grain boundary energy in nanoscale 10YSZ is expected to impact fracture toughness[12] since higher energy boundaries are expected to be mechanically weaker.[2,13] Analysis of the SEM images of the hardness indentation impressions shows significant differences when comparing samples with grain sizes larger and smaller than the size with maximum hardness (see Figure 5). For relatively large grains (48 nm), the corner cracks are fairly short (about 4.5 μm), whereas their sizes roughly double up to 8 μm for small grains (17 nm). This is an interesting observation since it is generally expected that fracture toughness increases with decreasing grain size, which would lead

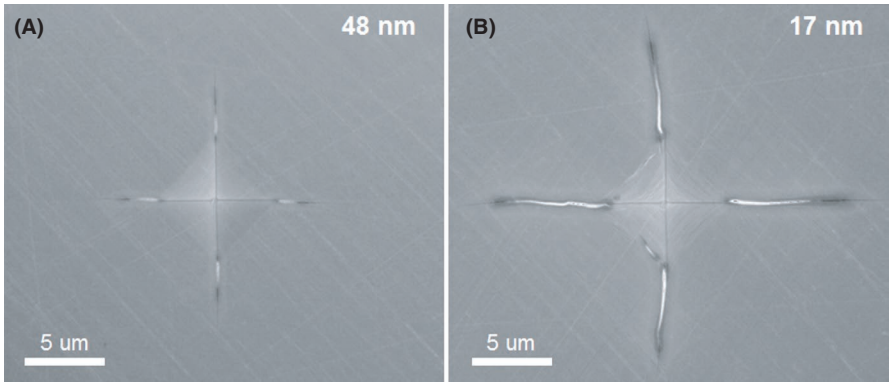

FIGURE 5 SEM images of typical hardness indentation impressions (60 gf) on the surface of 10YSZ samples with 48 nm (A) and 17 nm (B) grain size

to shorter corner cracks on the indents of the small grained sample.[33] This observation is however aligned with the fact that grain boundaries for the small grained sample were measured to have higher energies, as discussed in the previous session, making them mechanically weaker.

To further understand the energy accommodation mechanisms upon indentation, the indents for the 48 and 17 nm samples were laterally sectioned by focused ion beam to observe the microstructure at the subsurface region.

Sectioning was performed from across the indentation, allowing visualization of the cracks patterns underneath the top corner cracks observed in Figure 5 from their tips to the center of the indentation. As can be seen in Figure 6A-C, the 48 nm sample demonstrates crack pattern that resembles radial-like fracture at the front crack.[34] The cracks are indicated by an arrow in Figure 6C, and is fairly straight and planar across the sample, and this suggests fracture geometry consistent with the stress field generated by the load as described by Lawn and Swain.[35] The crack propagation occurs along the trajectory of lesser normal stress, nearly orthogonal to the main tensile component of the load. There is an absence of lateral vents or those are located underneath the images areas given the limited FIBed section, and Figure 6C shows the existence of a plastic deformation region located immediately underneath the center of the indentation, in which no cracks are observed. In contrast, the 17 nm sample shows a different pattern, which could be attributed to lateral cracking[36] (Figure 6D-F). Chen[36] defines that lateral cracks usually originate during the unloading cycle (for most ceramics), but for some glasses they also occur during the loading cycle. The fact that such lateral cracks are not observed or are present to a lesser extent for the 48 nm sample suggests the grain size is promoting lateral cracking.

Figure 7A,B shows TEM images of the cracks formed in both the 48 and 17 nm samples during in situ mechanical tests. For the 48 nm (B), one can differentiate the grains and observe that cracks are formed around grains, consistent with intergranular fracture. This contrasts with the apparent linearity (at the microscale) shown in Figure 6A-C, which could suggest transgranular failure, revealing conclusions

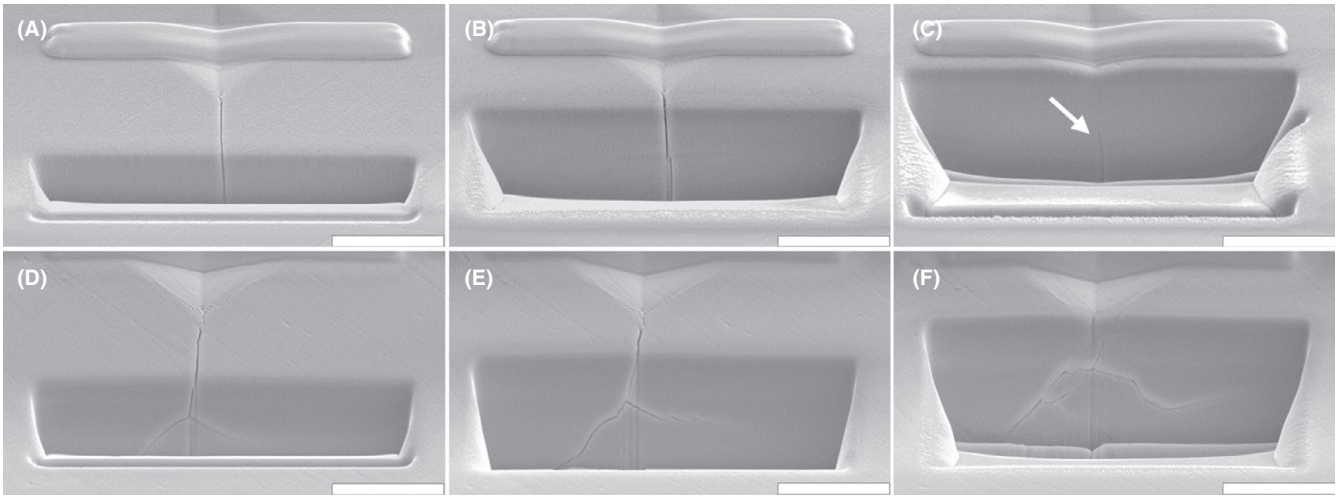

FIGURE 6 Sectioned hardness impressions prepared by FIB for 48 nm (A-C) and 17 nm (D-F) samples of 10YSZ imaged under SEM. The size of the scale bar is 10 microns

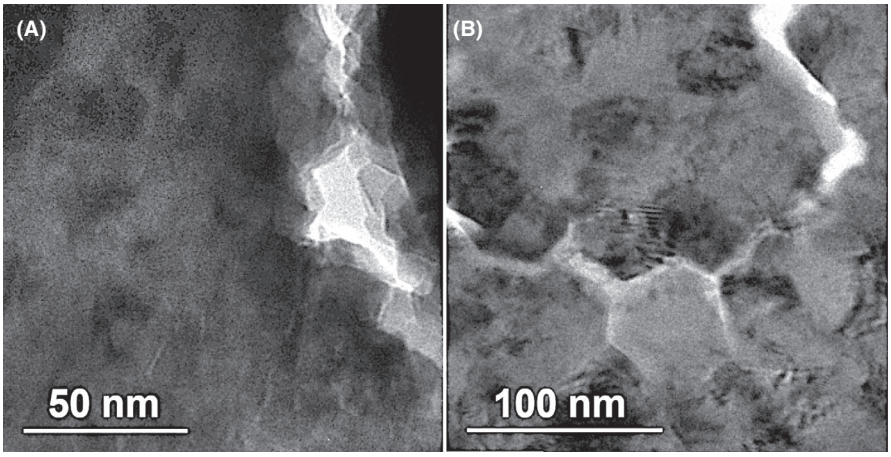

FIGURE 7 TEM images of cracks on FIB thinned nanoceramics for 17 nm (A) and 48 nm (B) samples of 10YSZ

based on low magnification images can be misleading when analyzing nanocrystalline materials. For the 17 nm sample, the grains are not well defined due to microscopy limitations, but the formed crack does appear to have features of grain contours, also suggesting intergranular fracture. This result implies there is no change in cracking mechanism between the two sizes, which is aligned with the hypothesis that the strength of the grain boundary network is responsible for the change in the fracture patterns observed underneath the indentation.

This observation goes against a recent observation by Yang et al who have demonstrated for $ZnAl_2O_4$ that a reduction in grain size leads to a change from transgranular to intergranular sub-surface fracture during indentation.[37] This mechanistic change is not observed in YSZ nanoceramics, at least in the studied grain size range. Although many functions may be affecting crack behavior, one may speculate that the existence of transgranular fracture in $ZnAl_2O_4$ is related to the capability of spinels, such as $MgAl_2O_4$, to present site inversion at the grain boundaries, which could lead to mechanically strengthening,[38] but this needs to be more systematically studied.

The observed decrease in hardness which is somehow associated with increasing grain boundary energy can be rather detrimental for some engineering purposes. It is therefore tempting to speculate that this behavior could be mitigated with the thermodynamic design of interfaces (lowering the grain boundary energies, for instance). As it has been demonstrated for the cubic YSZ system, La ions segregated at the interfaces can considerably decrease grain boundary energy and increase toughness of the entire grain boundary network.[12,15] Therefore, it could be expected that the increase in stability of grain boundaries can suppress the shear of grains and mitigate softening behavior, but this remains to be demonstrated.

4 | CONCLUSIONS

This study experimentally demonstrates that grain boundary energy is a function of grain size in 10YSZ and experiences a sudden increase when the size of the grains is below ~36 nm. The observed evolution of grain boundary energy coincides with the onset of the decrease in hardness, known as the inverse Hall-Petch relation. Analysis of sub-surface damage after hardness tests showed signs of intergranular fracture induced by indentation for samples before and after the hardness maximum. This indicates there is no change in load accommodation mechanism as a function of grain size, but as the grain boundary energy increases, grain boundaries become weaker and more prone to fracture, leading to softening in YSZ nanoceramics.

ACKNOWLEDGMENTS

The experimental work was financially supported by the Army Research Office Grant W911NF-17-1-0026. JRN thanks CNPq PDE Proc.303569/2015-8.

ORCID

Arseniy Bokov https://orcid.org/0000-0002-0293-8225
Ricardo H. R. Castro https://orcid.org/0000-0002-7574-7665

REFERENCES

1. Mitchell TE, Lagerlöf KPD, Heuer AH. Dislocations in ceramics. Mater Sci Technol. 1985;1:944–9.
2. Hu J, Shi YN, Sauvage X, Sha G, Lu K. Grain boundary stability governs hardening and softening in extremely fine nanograined metals. Science. 2017;355:1292–6.
3. Wollmershauser JA, Feigelson BN, Gorzkowski EP, Ellis CT, Goswami R, Qadri SB, et al. An extended hardness limit in bulk nanoceramics. Acta Mater. 2014;69:9–16.
4. Wang N, Wang Z, Aust KT, Erb U. Effect of grain size on mechanical properties of nanocrystalline materials. Acta Metall Mater. 1995;43:519–28.
5. Ryou H, Drazin JW, Wahl KJ, Qadri SB, Gorzkowski EP, Feigelson BN, et al. Below the Hall-Petch limit in nanocrystalline ceramics. ACS Nano. 2018;12:3083–94.
6. Ehre D, Chaim R. Abnormal Hall-Petch behavior in nanocrystalline MgO ceramic. J Mater Sci. 2008;43:6139–43.
7. Sokol M, Halabi M, Mordekovitz Y, Kalabukhov S, Hayun S, Frage N. An inverse Hall-Petch relation in nanocrystalline $MgAl_2O_4$ spinel consolidated by high pressure spark plasma sintering (HPSPS). Scr Mater. 2017;139:159–61.
8. Qi ZB, Sun P, Zhu FP, Wang ZC, Peng DL, Wu CH. The inverse Hall-Petch effect in nanocrystalline ZrN coatings. Surf Coatings Technol. 2011;205:3692–7.
9. Hahn EN, Meyers MA. Grain-size dependent mechanical behavior of nanocrystalline metals. Mater Sci Eng A. 2005;646:101–34.
10. Rohrer GS. Measuring and interpreting the structure of grain-boundary networks. J Am Ceram Soc. 2011;94:633–46.
11. Rohrer GS. Grain boundary energy anisotropy: a review. J Mater Sci. 2011;46:5881–95.
12. Bokov A, Zhang S, Feng L, Dillon SJ, Faller R, Castro RHR. Energetic design of grain boundary networks for toughening of nanocrystalline oxides. J Eur Ceram Soc. 2018;38:4260–7.
13. Tsurekawa S, Tanaka T, Yoshinaga H. Grain boundary structure, energy and strength in molybdenum. Mater Sci Eng A. 1994;176:341–8.
14. Drazin JW, Castro RHR. Phase stability in nanocrystals: a predictive diagram for yttria-zirconia. J Am Ceram Soc. 2015;98:1377–84.
15. Dey S, Chang C, Gong M, Liu F, Castro RHR. Grain growth resistant nanocrystalline zirconia by targeting zero grain boundary energies. J Mater Res. 2015;30:2991–3002.
16. Quach DV, Castro RHR. Direct measurement of grain boundary enthalpy of cubic yttria-stabilized zirconia by differential scanning calorimetry. J Appl Phys. 2012;112:083527.
17. Terwilliger CD, Chiang Y-M. Measurements of excess enthalpy in ultrafine-grained titanium dioxide. J Am Ceram Soc. 1995;78:2045–55.

18. Bokov A, Aguiar JA, Gong ML, Nikonov A, Castro RHR. A strategy to mitigate grain boundary blocking in nanocrystalline zirconia. J Phys Chem C. 2018;122:26344–52.
19. Saowadee N, Agersted K, Bowen JR. Effects of focused ion beam milling on electron backscatter diffraction patterns in strontium titanate and stabilized zirconia. J Microsc. 2012;246:279–86.
20. Sickafus KE, Hj M, Hartmanna TH, Yasudac K, Valdeza JA, Chodak P III, et al. Radiation damage effects in zirconia. J Nucl Mater. 1999;274:66–77.
21. Dey S, Drazin JW, Yang Y, Valdez JA, Holesinger TG, Uberuaga BP, et al. Radiation tolerance of nanocrystalline ceramics: insights from yttria stabilized zirconia. Sci Rep. 2015;5:7746.
22. Castro RHR, Torres RB, Pereira GJ, Gouvea D. Interface energy measurement of MgO and ZnO: understanding the thermodynamic stability of nanoparticles. Chem Mater. 2010;22:2502–9.
23. Mendelson MI. Average grain size in polycrystalline ceramics. J Am Ceram Soc. 1969;52:443–6.
24. Scherrer B, Heiroth S, Hafner R, Martynczuk J, Bieberle-Hütter A, Rupp JLM, et al. Crystallization and microstructure of yttria-stabilized-zirconia thin films deposited by spray pyrolysis. Adv Funct Mater. 2011;21:3967–75.
25. Vonlanthen P, Grobety B. CSL grain boundary distribution in alumina and zirconia ceramics. Ceram Int. 2008;34:1459–72.
26. Shibata N, Oba F, Yamamoto T, Ikuhara Y. Structure, energy and solute segregation behaviour of [110] symmetric tilt grain boundaries in yttria-stabilized cubic zirconia. Philos Mag. 2004;84:2381–415.
27. Kini MK. Grain boundary crystallography in polycrystalline yttria-stabilised cubic zirconia. Philos Mag. 2018;98:1865–83.
28. Frechero MA, Rocci M, Sanchez-Santolino G, Kumar A, Salafranca J, Schmidt R, et al. Paving the way to nanoionics: atomic origin of barriers for ionic transport through interfaces. Sci Rep. 2015;5:17229.
29. Chaim R. Percolative composite model for prediction of the properties of nanocrystalline materials. J Mater Res. 1997;12:1828–36.
30. Muche DNF, Marple MAT, Sen S, Castro RHR. Grain boundary energy, disordering energy and grain growth kinetics in nanocrystalline $MgAl_2O_4$ spinel. Acta Mater. 2018;149:302–11.
31. Kumar KS, van Swygenhoven H, Suresh S. Mechanical behavior of nanocrystalline metals and alloys. Acta Mater. 2003;51:5743–74.
32. Dao M, Lu L, Asaro R, Dehosson J, Ma E. Toward a quantitative understanding of mechanical behavior of nanocrystalline metals. Acta Mater. 2007;55:4041–65.
33. Foulk JW, Johnson GC, Klein PA, Ritchie RO. On the toughening of brittle materials by grain bridging: promoting intergranular fracture through grain angle, strength, and toughness. J Mech Phys Solids. 2008;56:2381–400.
34. Cook R, Pharr G. Direct observation and analysis of indentation cracking in glasses and ceramics. J Am Ceram Soc. 1990;73:787–817.
35. Lawn BR, Swain MV. Microfracture beneath point indentations in brittle solids. J Mater Sci. 1975;10:113–22.
36. Chen J. Indentation-based methods to assess fracture toughness for thin coatings. J Phys D: Appl Phys. 2012;45:1–14.
37. Yang C, Thron A, Castro RHR. Grain boundary strengthening in nanocrystalline zinc aluminate. J Am Ceram Soc. 2019;102(11):6904–12.
38. Muche DNF, Marple MAT, Hung I, Gan Z, Castro RHR, Sen S. Size-induced structural disorder enables ultrahard oxides. J Phys Chem C. 2017;121:13898–905.

How to cite this article: Bokov A, Rodrigues Neto JB, Lin F, Castro RHR. Size-induced grain boundary energy increase may cause softening of nanocrystalline yttria-stabilized zirconia. *J Am Ceram Soc*. 2019;00:1–11. https://doi.org/10.1111/jace.16886